INTERNATIONAL JOURNAL FOR NUMERICAL METHODS IN ENGINEERING
Int. J. Numer. Meth. Engng 2002; **54**:1751–1774 (DOI: 10.1002/nme.491)

A general and efficient formulation of fractures and boundary conditions in the finite element method

Ruben Juanes[‡], Javier Samper[*,†] and Jorge Molinero

Escuela de Ingenieros de Caminos, Canales y Puertos, Universidad de La Coruña, Campus de Elviña, 15192 La Coruña, Spain

SUMMARY

The need to assess quantitatively the safety of waste repositories in deep geological media has fostered the development of efficient numerical models of groundwater flow and contaminant transport in fractured media. These models usually account for water flow through fracture zones embedded in a 3D rock matrix continuum. The first formulation of fractures in groundwater flow finite element models was proposed by Kiraly, and later revisited and generalized by Perrochet. From a mathematical viewpoint, fractures can be considered as m-dimensional manifolds in an n-dimensional Euclidean space ($m \leqslant n$). The key step of this formulation lies in an expression relating the hypersurface element $\mathrm{d}S_m$ to the infinitesimal local co-ordinates $\mathrm{d}\xi_i$ ($i = 1, \ldots, m$). Here we present a novel proof for this relation using a different approach to that of Perrochet, and explore the efficiency and accuracy of the formulation. It is shown that the aforementioned relation leads to a general and compact formulation which is not only applicable to elements of any dimension (e.g. 1D, 2D and 3D elements in a 3D domain), but also overcomes the cumbersome and case-specific calculations of traditional approaches. This formulation has been implemented in a versatile finite element program for modelling groundwater flow, solute transport and heat transport in porous and fractured media. The efficiency and accuracy of the proposed formulation has been analysed using a synthetic case dealing with flow and solute transport through a 2D fractured rock block. The proposed formulation, in which fractures are discretized by means of 1D elements is more efficient and accurate than the traditional finite element formulation of discretizing fractures by means of 2D elements. The capability of the proposed formulation to cope with complex systems is illustrated with a case study of groundwater flow induced by the construction of the access tunnel to an underground research laboratory in Äspö (Sweden). The numerical model is able to reproduce the observed records of water levels in boreholes and flow rates into the tunnel. Although the proposed formulation has been implemented and tested within the framework of groundwater flow and solute transport in fractured porous media, it should be of interest for other boundary value problems.

KEY WORDS: finite element method; fractures; manifolds; groundwater flow; solute transport

*Correspondence to: Javier Samper, Escuela de Ingenieros de Caminos, Canales y Puertos, Universidad de La Coruña, Campus de Elviña, 15192 La Coruña, Spain.
†E-mail: samper@iccp.udc.es
‡Now at the Department of Civil and Environmental Engineering, University of California at Berkeley, 631 Davis Hall, Berkeley CA 94720-1710, U.S.A.

Contract/grant sponsor: ENRESA (Spanish Agency for Nuclear Waste). European Commission; contract/grant number: F14W-CT95-0006.
Contract/grant sponsor: CICYT; contract/grant number: HID98-282.

Received 2 October 2000
Revised 10 August 2001

1. INTRODUCTION

Three-dimensional numerical models of groundwater flow and solute transport through fractured porous media are required for groundwater resources management and for the evaluation of the fate of groundwater pollution by toxic wastes. While most of the flow occurs along fractures, the rock matrix plays a major role in retarding the migration of contaminants. Different conceptual models have been proposed in the literature for flow and transport in fractured media (see, e.g. the summary in Reference [1] and the references therein). There is a consensus on the fact that the embedded fracture model (according to which fractures are discretized as geometrical entities embedded in a continuum) is the most appropriate model for systems containing major fracture zones.

There are two numerical approaches for embedding fractures within the continuum: (1) by discretizing fractures with distorted three-dimensional elements in a three-dimensional medium and (2) by treating fractures as two-dimensional surfaces in a three-dimensional space. As it is shown in this paper, the latter approach is more natural and numerically much more efficient.

The idea of representing fractures with elements of lower dimensions first appeared in Reference [2]. In this pioneer work, steady-state groundwater flow was simulated in a highly fractured hydrogeological system. The same model was later revisited in subsequent articles [3, 4]. Based on this idea, Perrochet [5] developed a method for the evaluation of finite element matrices in a 4D geometrical framework, and used this formulation in conjunction with space–time techniques. As an application of the method he considered a pure convection problem on a 2D manifold with curvature in a 3D space. He reported excellent results using a stabilized space–time finite element formulation. In this context, the need for domains of dimension higher than three is evident.

In view of the great potential interest of this embedded manifold formulation in subsurface hydrology and possibly many other fields of engineering, the present paper points out some relevant issues not addressed in previous references.

While Reference [5] devotes much attention to the computation of gradients in global co-ordinates, the problem of integration on manifolds is not discussed in detail. The key point for the computation of integrals over m-dimensional surfaces within n-dimensional Euclidean spaces ($m \leqslant n$) lies on a general expression relating the differential of a generalized surface $\mathrm{d}S_m$ (hypersurface element) in global co-ordinates to the differential of local co-ordinates $\mathrm{d}\xi_i$ ($i = 1, \ldots, m$). This expression, which does not seem to be well known among the finite element community, is stated in Reference [5] without a proof. In this paper we provide a novel proof for such expression, which is used here for computing integrals over fractures embedded in a continuum *and* for evaluating integrals along boundaries. This permits a unified treatment of element and boundary integrals in finite element formulations, which is of practical interest even in the absence of fractures. The formulation has been implemented in a computer code, which solves the equations of groundwater flow, solute transport and heat transfer through porous and fractured media, thus extending the range of problems tackled by Kiraly and co-workers [2–4].

The embedded manifold approach is not only more general, compact and elegant than traditional formulations, as acknowledged in earlier works. In this paper we show, by means of a realistic synthetic case, that it can also lead to much more efficient numerical solutions. The test case simulates solute transport through a rectangular porous block with a network

of interconnected orthogonal fractures. An extensive comparison is performed between the numerical performance of the proposed formulation and that of the traditional formulation. Significantly more accurate solutions are obtained with a much less computational cost when fractures are discretized with 1D elements.

A real case study is also presented to illustrate the potential of the proposed approach for practical applications. It deals with three-dimensional flow in a fractured rock induced by the construction of a tunnel. This study differs from the application example in Reference [3] in that: (1) the scale is of the order of kilometers (field scale) and not hundreds of kilometers (regional scale), (2) the model is fully transient due to the advancing tunnel front, (3) solute transport is modelled in addition to groundwater flow and (4) the model in Reference [3] was used to 'analyse the sensitivity of the solution to hypotheses' whereas in the present case the model was calibrated with measured data and used successfully as a predictive tool.

The paper is organized as follows: in Section 2 the mathematical and finite element formulations of groundwater flow and solute transport are presented. Section 3 addresses the problem of integrating on a manifold, including an original proof of the expression for the hypersurface element. The pseudocode for the implementation of the proposed formulation in a finite element program is described in Section 4. The test case in Section 5 and the real case study in Section 6 illustrate the efficiency and applicability of the formulation. The most salient findings are summarized in the conclusions.

2. THE MATHEMATICAL PROBLEM

The physical processes of groundwater flow and solute transport can be modelled mathematically as initial and boundary value problems [6], which may be expressed in a general form as the partial differential equation

$$\frac{\partial u}{\partial t} + \mathscr{L}(u) = f \quad \text{in } \Omega,\ t \in (0, T) \tag{1}$$

where u is the scalar unknown, $\mathscr{L}(\cdot)$ is a differential operator describing the physical process, f is a problem-dependent source term, $\Omega \subset \mathbb{R}^d$ is the spatial domain and $(0, T)$ is the time interval of interest. The space dimension will usually be $d = 2, 3$. The differential operator takes the form of the scalar advection–diffusion-reaction equation:

$$\begin{aligned} \mathscr{L}(u) &:= -\nabla \cdot (\mathbf{a} \nabla u) + \mathbf{b} \cdot \nabla u + cu \\ &= -\sum_{i,j} \frac{\partial}{\partial x_i} \left(a_{ij} \frac{\partial u}{\partial x_j} \right) + \sum_j b_j \frac{\partial u}{\partial x_j} + cu \end{aligned} \tag{2}$$

where $\mathbf{a} = [a_{ij}]$ is the diffusion tensor (assumed symmetric positive definite), $\mathbf{b} = \{b_j\}$ is the advective velocity, and c is the absorption coefficient. Three different types of boundary conditions are considered, namely, essential (Dirichlet), natural (Neumann) and mixed (Cauchy). Let $\partial\Omega$ be the boundary of the domain, and $\Gamma \subset \partial\Omega$ the part of the boundary on which essential boundary conditions are imposed (assume $\Gamma \neq \emptyset$). The boundary conditions of the problem

Table I. Partial differential equations of: (1) groundwater flow and (2) solute transport, with the corresponding boundary conditions.

Process	Differential equation	Mixed type BC
(1)	$S_s \frac{\partial h}{\partial t} - \nabla \cdot (\mathbf{K} \nabla h) = r$	$-(\mathbf{K} \nabla h) \cdot \mathbf{n} = Q + \alpha(h - \tilde{h})$
(2)	$\phi R \frac{\partial c}{\partial t} - \nabla \cdot (\phi \mathbf{D} \nabla c) + \mathbf{q} \cdot \nabla c + \lambda \phi R c = r(\tilde{c} - c)$	$-(\phi \mathbf{D} \nabla c) \cdot \mathbf{n} = F + \beta(c - \tilde{c})$

(1) Groundwater flow

h	Piezometric head (L)
t	Time (T)
$\mathbf{K}$	Hydraulic conductivity tensor ($\mathrm{L\,T^{-1}}$)
r	Volumetric recharge ($\mathrm{T^{-1}}$)
S_s	Specific storage coefficient ($\mathrm{L^{-1}}$)
$\mathbf{n}$	Outward unit normal vector (dimensionless)
α	Leakage coefficient ($\mathrm{T^{-1}}$)
$\tilde{h}$	External piezometric head on the boundary (L)
Q	Flow rate across boundary per unit area ($\mathrm{L\,T^{-1}}$)

(2) Solute transport

c	Concentration ($\mathrm{M\,L^{-3}}$)
ϕ	Porosity, (dimensionless)
$\mathbf{D}$	Diffusion–dispersion tensor ($\mathrm{L^2\,T^{-1}}$)
$\mathbf{q}$	Darcy velocity vector ($\mathrm{L\,T^{-1}}$)
λ	Radioactive decay constant ($\mathrm{T^{-1}}$)
R	Retardation coefficient (dimensionless)
β	Solute transfer coefficient ($\mathrm{L\,T^{-1}}$)
$\tilde{c}$	External concentration on the boundary ($\mathrm{ML^{-3}}$)
F	Imposed dispersive flux on the boundary ($\mathrm{M\,L^{-2}\,T^{-1}}$)

are expressed as

$$u = \tilde{u} \quad \text{on } \Gamma, \ t \in (0, T) \tag{3}$$

$$-(\mathbf{a} \nabla u) \cdot \mathbf{n} = g + k(u - \tilde{u}) \quad \text{on } \partial\Omega \backslash \Gamma, \ t \in (0, T) \tag{4}$$

where $\tilde{u}$ is the specified value of the variable on the boundary, $\mathbf{n}$ is the outward unit normal vector, g is the flux across the boundary, and k is a transfer coefficient. Natural boundary conditions are in fact a particular case of boundary conditions of the mixed type, where $k = 0$. The complete definition of the problem requires knowing the initial conditions

$$u = u_0 \quad \text{in } \Omega, \ t = 0 \tag{5}$$

Table I contains the actual expressions of the generic partial differential equation and mixed boundary conditions for the problems of groundwater flow and solute transport.

For obtaining the weak form of the problem given by the differential equation (1)–(2), with the boundary conditions (3)–(4) and the initial condition (5), it is convenient to introduce the following function spaces:

$$\mathscr{V} := \{v \in H^1(\Omega):\ v = 0 \text{ on } \Gamma\} \tag{6}$$

$$\tilde{\mathscr{V}} := \{v \in H^1(\Omega):\ v = \tilde{u} \text{ on } \Gamma\} \tag{7}$$

where $H^1(\Omega)$ is the usual Sobolev space of functions which are square integrable and have square integrable first derivatives. The weak form of the original problem reduces to find $u \in \tilde{\mathscr{V}}$ for each fixed t, such that

$$\left(\frac{\partial u}{\partial t}, v\right) + a(u, v) = l(v) \quad \forall v \in \mathscr{V},\ \ u(x, 0) = u_0(x) \tag{8}$$

where

$$\left(\frac{\partial u}{\partial t}, v\right) = \int_\Omega \frac{\partial u}{\partial t}\, v \, \mathrm{d}x$$

$$a(u, v) = \int_\Omega (\mathbf{a}\nabla u) \cdot \nabla v \, \mathrm{d}x + \int_\Omega (\mathbf{b} \cdot \nabla u) v \, \mathrm{d}x + \int_\Omega cuv \, \mathrm{d}x + \int_{\partial\Omega\setminus\Gamma} kuv \, \mathrm{d}s$$

$$l(v) = \int_\Omega fv \, \mathrm{d}x + \int_{\partial\Omega\setminus\Gamma} gv \, \mathrm{d}s + \int_{\partial\Omega\setminus\Gamma} k\tilde{u}v \, \mathrm{d}s$$

A standard Galerkin finite element formulation is used to obtain a semidiscrete problem of the weak form (8). In matrix notation this may be expressed as

$$\mathbf{M}\mathbf{u}' + \mathbf{K}\mathbf{u} = \mathbf{l}, \quad \boldsymbol{\alpha}(0) = \boldsymbol{\alpha}_0 \tag{9}$$

where $\mathbf{M}$ is the 'mass' matrix, $\mathbf{K}$ is the 'stiffness' matrix, $\mathbf{l}$ is the right-hand side vector, $\mathbf{u}$ is the vector of unknowns and $\boldsymbol{\alpha}_0$ defines the initial conditions. It is worth noting that matrices $\mathbf{M}$ and $\mathbf{K}$ are obtained by assembling element matrices, which in turn requires evaluating integrals over elements and element boundaries. The fully discrete problem is then obtained by further discretizing in time the (usually very stiff) system of ordinary differential equations (9). A detailed description and analysis of the finite element method can be found elsewhere [7–9].

3. INTEGRATION OVER SURFACES

The finite element method for solving boundary value problems requires the computation of integrals over the domain Ω and its boundary $\partial\Omega$ (see Equation (8)). Owing to the local character of the basis functions, these integrals can be calculated as sums of integrals over the elements. Integrands are usually expressed in terms of local (natural) co-ordinates through the trial and test functions.

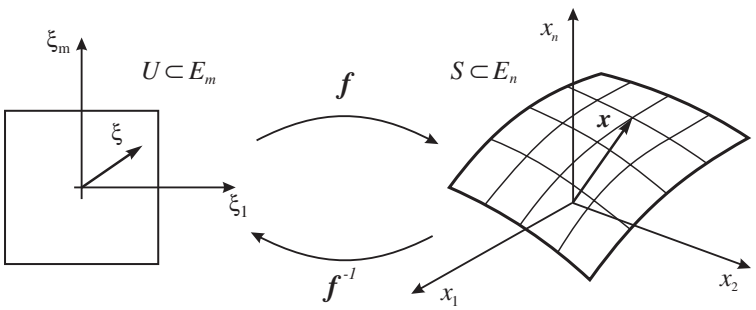

Figure 1. Mapping of set $U \subset E_m$ onto surface $S \subset E_n$.

The standard finite element method [10] works only when the local-to-global mapping has an invertible Jacobian. In particular, this requirement implies that the dimension of the reference element is the same as that of the domain. This is not the case when integrating over elements representing fractures or deviated wells, element boundaries, and in the context of space–time formulations [5]. A method for evaluating integrals over m-dimensional surfaces in $\mathbb{R}^n$ $(m \leqslant n)$ is required to avoid specific calculations for each case.

The definition of a generalized surface (hypersurface or manifold) is established clearly in Courant and John [11]. Let E_n be a n-dimensional Euclidean space with (Cartesian) co-ordinates $\mathbf{x} = (x_1, \ldots, x_n)$. A set S in E_n is a m-dimensional surface if one can find n functions

$$\begin{aligned} \mathbf{f} &: U \subset E_m \to S \subset E_n \\ \boldsymbol{\xi} &\mapsto \mathbf{x} = \mathbf{f}(\boldsymbol{\xi}) \end{aligned} \tag{10}$$

defined in an open set U of the space E_m with (local) co-ordinates $\boldsymbol{\xi} = (\xi_1, \ldots, \xi_m)$ (see Figure 1) with the following properties:

1. Equations $\mathbf{x} = \mathbf{f}(\boldsymbol{\xi})$ define a one-to-one continuous mapping of U onto S, whose inverse is also continuous.
2. Functions $f_i(\xi_1, \ldots, \xi_m)$ have continuous first derivatives in U.
3. At any point $\boldsymbol{\xi} \in U$, the m vectors in E_n

$$\mathbf{A}_i(\boldsymbol{\xi}) := \frac{\partial \mathbf{f}}{\partial \xi_i} \tag{11}$$

are independent, that is,

$$\sqrt{\Gamma(\mathbf{A}_1, \mathbf{A}_2, \ldots, \mathbf{A}_m)} = \sqrt{\det(\mathbf{G}_m)} > 0$$

where $\mathbf{G}_m$ is the covariant metric tensor of the mapping and Γ is the Gram determinant, defined as [11]:

$$\Gamma(\mathbf{A}_1, \mathbf{A}_2, \ldots, \mathbf{A}_m) = \det(\mathbf{G}_m) = \det \begin{pmatrix} \mathbf{A}_1 \cdot \mathbf{A}_1 & \cdots & \mathbf{A}_1 \cdot \mathbf{A}_m \\ \vdots & & \vdots \\ \mathbf{A}_m \cdot \mathbf{A}_1 & \cdots & \mathbf{A}_m \cdot \mathbf{A}_m \end{pmatrix} \tag{12}$$

In general, the integral of a continuous function $F(\mathbf{x}) = F(x_1, \ldots, x_n)$ defined on a hypersurface S in the global space E_n (co-ordinates $\mathbf{x}$) is defined as

$$\int_S F(\mathbf{x})\, \mathrm{d}S = \int_U F(\mathbf{x}(\boldsymbol{\xi}))\, \mathrm{d}S_m \tag{13}$$

where $U \subset E_m$ is an open set in the local space (co-ordinates $\boldsymbol{\xi}$). The key point for the computation of the integral lies in relating the differential of the m-dimensional surface $\mathrm{d}S_m$ in an n-dimensional Euclidean space E_n to the differential of the local co-ordinates $\mathrm{d}\xi_1, \ldots, \mathrm{d}\xi_m$. Such a relation is given by

$$\mathrm{d}S_m = \sqrt{\det(\mathbf{G}_m)}\, \mathrm{d}\xi_1\, \mathrm{d}\xi_2 \cdots \mathrm{d}\xi_m \quad \text{for } 1 \leqslant m \leqslant n \tag{14}$$

where $\mathbf{G}_m$ is the covariant metric tensor of the mapping $\boldsymbol{\xi} \xrightarrow{\mathbf{f}} \mathbf{x}$, defined in Equation (12). Note that, with the definition above, the integral does not depend on the specific parametric representation of S [11, 12]. Equations (13) and (14) constitute the kernel of the proposed formulation for the efficient evaluation of boundary integrals and integrals over fractures embedded in a continuum.

Equation (14) was presented in Reference [5] with a different notation. However, a proof was not given. Reference [13], which is the standard reference for the mathematical developments in Reference [5], does not provide a proof either. A proof of Equation (14) is given in Reference [11] only for the case of $m = n - 1$. A more academic approach may be found in Reference [12] for the general case $m \leqslant n$, where a non-constructive proof is presented.

A novel proof of Equation (14) for computing integrals over a m-dimensional manifold $S \subset E_n$ is presented here. It follows an induction process, where

1. For $m = 1$ (infinitesimal arc length), one has

$$\mathrm{d}S_1 = \mathrm{d}\ell = \sqrt{\det(\mathbf{G}_1)}\, \mathrm{d}\xi_1$$

2. Given that for a m-dimensional surface, Equation (14) holds true, then one can prove that

$$\mathrm{d}S_{m+1} = \sqrt{\det(\mathbf{G}_{m+1})}\, \mathrm{d}\xi_1\, \mathrm{d}\xi_2 \cdots \mathrm{d}\xi_{m+1} \tag{15}$$

Proof of this last step is based on the fact that the $(m+1)$-dimensional hypersurface element dS_{m+1} may be obtained with generality from $\mathrm{d}S_m$ as

$$\mathrm{d}S_{m+1} = \mathrm{d}h\, \mathrm{d}S_m \tag{16}$$

where $\mathrm{d}h$ is the length of vector $\mathrm{d}\mathbf{h}$ in the n-dimensional Euclidean space $\mathbb{R}^n$. Vector $\mathrm{d}\mathbf{h}$ is by definition, normal to the hyperplane tangent to the surface S_m at point $\mathbf{x}$.

Let $\{\mathrm{d}\mathbf{x}_i\}$ $(i = 1, \ldots, m)$ be a set of independent vectors that span the hyperplane tangent to the m-dimensional surface S_m at point $\mathbf{x} \in S_m$, where $\mathbf{x}$ is a vector of E_n (see Figure 2 for $m = 2$ and $n = 3$). Vectors $\mathrm{d}\mathbf{x}_i$ are computed by means of the following expression:

$$\mathrm{d}\mathbf{x}_i = \frac{\partial \mathbf{x}}{\partial \xi_i}\, \mathrm{d}\xi_i = \frac{\partial \mathbf{f}(\boldsymbol{\xi})}{\partial \xi_i}\, \mathrm{d}\xi_i = \mathbf{A}_i\, \mathrm{d}\xi_i, \quad i = 1, \ldots, m \tag{17}$$

according to the definition of $\mathbf{A}_i$ given in Equation (11). Similarly, one may define

$$\mathrm{d}\mathbf{x}_{m+1} = \mathbf{A}_{m+1}\, \mathrm{d}\xi_{m+1} \tag{18}$$

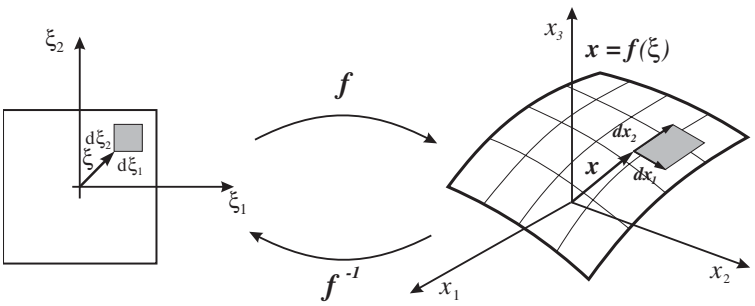

Figure 2. Tangent plane to a 2D surface $S \subset \mathbb{R}^3$, at a point $\mathbf{x} \in S$.

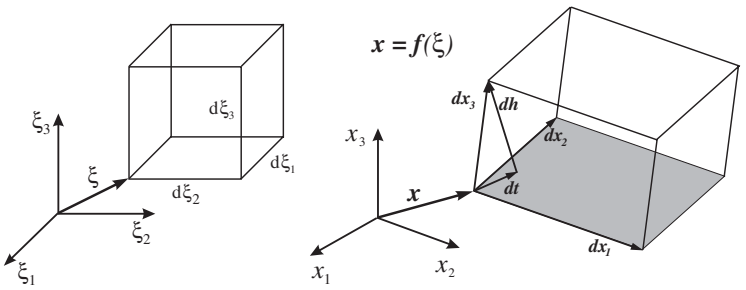

Figure 3. Geometrical interpretation of the hypersurface element $\mathrm{d}S_{m+1}$ for $m = 2$ and $n = 3$.

Vector $\mathrm{d}\mathbf{x}_{m+1}$ can be expressed as the sum of two vectors, $\mathrm{d}\mathbf{t}$ and $\mathrm{d}\mathbf{h}$, which are tangent and normal to the hyperplane tangent to S_m, respectively (see Figure 3 for $m = 2$ and $n = 3$):

$$\mathrm{d}\mathbf{x}_{m+1} = \mathrm{d}\mathbf{t} + \mathrm{d}\mathbf{h} \tag{19}$$

Vector $\mathrm{d}\mathbf{t}$ can always be expressed as a linear combination of vectors $\mathrm{d}\mathbf{x}_1, \ldots, \mathrm{d}\mathbf{x}_m$, because $\mathrm{d}\mathbf{t}$ belongs to the hyperplane tangent to the surface. Therefore, it follows that

$$\mathrm{d}\mathbf{t} = \lambda_1 \, \mathrm{d}\mathbf{x}_1 + \cdots + \lambda_m \, \mathrm{d}\mathbf{x}_m \tag{20}$$

From Equations (18)–(20) one has

$$\mathrm{d}\mathbf{h} = \mathbf{A}_{m+1} \, \mathrm{d}\xi_{m+1} - \sum_{i=1}^{m} \lambda_i \, \mathrm{d}\mathbf{x}_i \tag{21}$$

The length of vector $\mathrm{d}\mathbf{h}$ can be computed through the expression

$$(\mathrm{d}h)^2 = \mathrm{d}\mathbf{h} \cdot \mathrm{d}\mathbf{h} \tag{22}$$

In addition, since vector $\mathrm{d}\mathbf{h}$ is normal to the hyperplane spanned by vectors $\mathrm{d}\mathbf{x}_1, \ldots, \mathrm{d}\mathbf{x}_m$, it follows that

$$\mathrm{d}\mathbf{h} \cdot \mathrm{d}\mathbf{x}_i = 0 \tag{23}$$

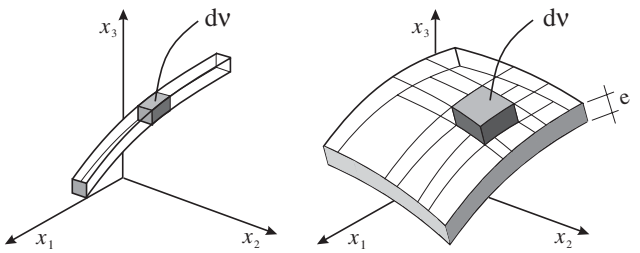

Figure 4. Differential volume $d\mathscr{V}$ in 1D and 2D fractures in a 3D space.

Using (14), (17), (21)–(23), Equation (16) leads to

$$(dS_{m+1})^2 = \left(\mathbf{A}_{m+1}\, d\xi_{m+1} \cdot \mathbf{A}_{m+1}\, d\xi_{m+1} - \sum_{i=1}^{m} \lambda_i \mathbf{A}_i\, d\xi_i \cdot \mathbf{A}_{m+1}\, d\xi_{m+1}\right) \Gamma(\mathbf{A}_1, \ldots, \mathbf{A}_m)(d\xi_1)^2 \cdots (d\xi_m)^2 \tag{24}$$

Using the properties of determinants, one can show that Equation (24) can be written as

$$(dS_{m+1})^2 = \Gamma(\mathbf{A}_1, \ldots, \mathbf{A}_{m+1})(d\xi_1)^2 \cdots (d\xi_{m+1})^2$$

or, equivalently,

$$dS_{m+1} = \sqrt{\det(\mathbf{G}_{m+1})}\, d\xi_1 \cdots d\xi_{m+1}$$

which completes the proof of Equation (15). The details of the calculation are presented in Reference [1], and have been omitted here.

Once the infinitesimal generalized surface dS_m has been obtained, the calculation of the differential volume $d\mathscr{V}$ in fractures (elements of lower dimension than the Euclidean space) is straightforward. It only requires multiplying by the cross-sectional area of the fracture for 1D elements and by the thickness for 2D elements (see Figure 4).

The finite element formulation involves also the computation of global derivatives of functions which are usually expressed in terms of local co-ordinates (such as the shape functions). Let

$$\phi = \phi(\boldsymbol{\xi}) = \phi(\xi_1, \ldots, \xi_m)$$

a straightforward calculation (see, e.g. References [1, 5]) gives the relation between the global derivatives $d\phi/d\mathbf{x}$ and the local derivatives $d\phi/d\boldsymbol{\xi}$ for points $\mathbf{x}$ *on the hypersurface* S:

$$\boldsymbol{\nabla}\phi = \left.\frac{d\phi}{d\mathbf{x}}\right|_{\mathbf{x}\in S} = \left.\frac{d\phi}{d\boldsymbol{\xi}}\mathbf{G}_m^{-1}\mathbf{J}_m^t\right|_{\mathbf{x}\in S}$$

In the equation above, $\mathbf{J}_m$ is the Jacobian matrix of the mapping of $U \subset E_m$ onto $S \subset E_n$ defined in Equation (10),

$$\underbrace{\mathbf{J}_m}_{n\times m} = \begin{pmatrix} \dfrac{\partial f_1}{\partial \xi_1} & \cdots & \dfrac{\partial f_1}{\partial \xi_m} \\ \vdots & & \vdots \\ \dfrac{\partial f_n}{\partial \xi_1} & \cdots & \dfrac{\partial f_n}{\partial \xi_m} \end{pmatrix}$$

Note that the covariant metric tensor can be expressed as

$$\underbrace{\mathbf{G}_m}_{m\times m} = \mathbf{J}_m^t \mathbf{J}_m$$

4. IMPLEMENTATION OF THE FORMULATION IN A COMPUTER CODE

The process of obtaining the different element matrices is briefly described in this section and applied, for the sake of clarity, to the matrix corresponding to the diffusive term of the flow equation. If the standard Galerkin formulation is used, the element matrix reads

$$\underbrace{\mathbf{A}^e}_{N_n\times N_n} = \int_{\Omega^e} \underbrace{\nabla\boldsymbol{\phi}}_{N_n\times n} \cdot \underbrace{\mathbf{K}}_{n\times n} \cdot \underbrace{\nabla\boldsymbol{\phi}^t}_{n\times N_n} \mathrm{d}x \tag{25}$$

where n is the dimension of the spatial domain, N_n is the number of nodes of the element, $\boldsymbol{\phi} = (\phi_1, \ldots, \phi_{N_n})^t$ is the vector of shape functions, and $\mathbf{K}$ is the hydraulic conductivity tensor. This integral, in general, cannot be computed analytically. The required steps to evaluate Equation (25) are presented below.

do $e = 1, N_e$ (loop over elements)

- Update nodal co-ordinates (ELCOD)

$$\underbrace{\mathbf{X}}_{N_n\times n} = \begin{pmatrix} x_{1,1} & \cdots & x_{1,n} \\ \vdots & & \vdots \\ x_{N_n,1} & \cdots & x_{N_n,n} \end{pmatrix}$$

do $g = 1, N_g$ (loop over Gauss points)

- Update Gauss points co-ordinates (POSGE): $\underbrace{\boldsymbol{\xi}_g}_{N_g} = (\xi_1, \ldots, \xi_m)_g$.
- Update Gauss points weights (WEIGE): w_g.
- Evaluate shape functions (SHAPE):

$$\underbrace{\boldsymbol{\phi}_g}_{N_n} = \begin{pmatrix} \phi_1(\boldsymbol{\xi}_g) \\ \vdots \\ \phi_{N_n}(\boldsymbol{\xi}_g) \end{pmatrix}$$

- Evaluate derivatives of the shape functions (DERIE):

$$\underbrace{\mathbf{E}_g}_{N_n\times m} = \begin{pmatrix} \dfrac{\partial\phi_1}{\partial\xi_1} & \cdots & \dfrac{\partial\phi_1}{\partial\xi_m} \\ \vdots & & \vdots \\ \dfrac{\partial\phi_{N_n}}{\partial\xi_1} & \cdots & \dfrac{\partial\phi_{N_n}}{\partial\xi_m} \end{pmatrix}_g$$

- Compute Jacobian matrix (XJACM): $\underbrace{\mathbf{J}_g}_{n\times m} = \underbrace{\mathbf{X}^t}_{n\times N_n}\underbrace{\mathbf{E}_g}_{N_n\times m}$
- Compute covariant metric tensor (XJACE): $\underbrace{\mathbf{G}_g}_{m\times m} = \underbrace{\mathbf{J}_g^t}_{m\times n}\underbrace{\mathbf{J}_g}_{n\times m}$
- Evaluate Cartesian derivatives (CARTD): $\underbrace{\mathbf{B}_g}_{N_n\times n} = \boldsymbol{\nabla}\boldsymbol{\phi}_g = \underbrace{\mathbf{E}_g}_{N_n\times m}\underbrace{\mathbf{G}_g^{-1}}_{m\times m}\underbrace{\mathbf{J}_g^t}_{m\times n}$
- Compute constitutive matrix (DMATX): $\underbrace{\mathbf{D}_g}_{n\times n} = \mathbf{K}$
- Compute differential volume (DVOLU):

$$\mathrm{d}\mathscr{V}_g = b\sqrt{\det(\mathbf{G})_g}\,w_g, \quad b = \begin{cases} \text{Area} & \text{for a 1D element} \\ \text{Thickness} & \text{for a 2D element} \\ 1 & \text{for a 3D element} \end{cases}$$

enddo g (end of loop over Gauss points)

- Compute integral (AMATF)

$$\underbrace{\mathbf{A}^e}_{N_n\times N_n} = \sum_{g=1}^{N_g} \underbrace{\mathbf{B}_g}_{N_n\times n}\underbrace{\mathbf{D}_g}_{n\times n}\underbrace{\mathbf{B}_g^t}_{n\times N_n}\,\mathrm{d}\mathscr{V}_g$$

enddo e (end of loop over elements)

The formulation presented in this paper has been implemented in a computer code, TRANMEF-3, which solves the equations of groundwater flow, multicomponent solute transport and heat transfer in fully three-dimensional fractured porous media by the finite element method. The code has been thoroughly verified against available (or developed) analytical solutions in hundreds of cases. A complete description of the code is presented in Reference [6].

5. TEST CASE: RECTANGULAR BLOCK WITH A NETWORK OF FRACTURES

5.1. Problem description

This example, which considers very realistic features of flow and transport in fractured media, serves to illustrate the potential of the proposed formulation to analyse real problems. This test case has been used also to compare the proposed numerical formulation with conventional finite element discretization schemes. Further verification and validation examples can be found in Reference [14].

The problem considers water flow and solute transport through a rectangular rock block with a network of interconnected orthogonal fractures, as shown in Figure 5. Both top and bottom boundaries are considered to be no-flow boundaries. Piezometric head is imposed on lateral boundaries ($h = 1$ m on the left boundary and $h = 0$ m on the right boundary) such that water flows from left to right. Water flows preferentially through the fractures, because they are more permeable than the rock matrix. Water flows under steady-state conditions. Solute concentration is initially zero over the entire domain. After time $t = 0$ water entering the domain through the left side of the fracture network has a concentration C_0.

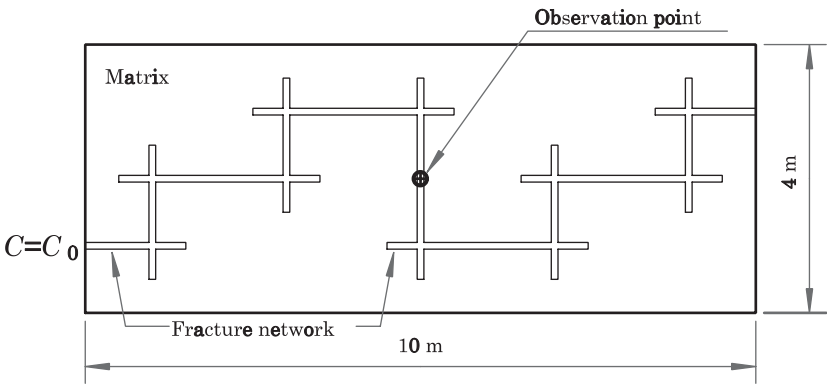

Figure 5. Sketch of the test case: rectangular block with a network of interconnected fractures.

Table II. Flow and transport parameters for the test case.

Parameter	Description	Matrix	Fracture
e	Thickness	1 m	1 m
$2b$	Fracture width	—	0.04 m
K	Hydraulic conductivity	10^{-5} m d^{-1}	10^{-2} m d^{-1}
S_s	Specific storage coeff.	10^{-6} m^{-1}	10^{-3} m^{-1}
ϕ	Porosity	0.01	0.1
α_L	Longitudinal dispersivity	10^{-2} m	5×10^{-2} m
α_T	Transverse dispersivity	2×10^{-3} m	10^{-2} m
D	Effective diffusion coeff.	10^{-6} m^2 d^{-1}	10^{-5} m^2 d^{-1}

5.2. *Numerical solution*

This test case has been solved using two different finite element discretization schemes. The so-called '2D model' makes use of the traditional finite element formulation, in which fractures are discretized with 2D elements. The '1D model' uses the formulation proposed in this paper, in which fractures are discretized by means of 1D elements. Numerical values of flow and transport parameters (for the rock matrix and the fractures) are shown in Table II. The concentration of the water at the inlet is $C_0 = 1$ mg l^{-1}.

Several runs have been carried out for both models using increasingly finer grids. The most relevant features of the different finite element grids, as well as the terminology used for later discussions, are shown in Table III.

Figure 6 shows one of the finite element grids used for the 2D Model, which has 2112 nodes. It should be noted that the mesh has been refined in the neighbourhood of the fractures, given the higher water velocity along the fracture zones and the dramatic change in the properties of the medium at the fracture–matrix interface. Grids used in the rest of the cases are similar to that shown in Figure 6. A detail of the mesh refinement around the fractures is shown in Figure 7 for the 2D Model with 18 149 nodes (left) and the 1D Model with 19 705 nodes (right). The latter represents fractures using 1D elements with an associated width of 0.04 m to ensure that fractures have the same transmissivity for both models.

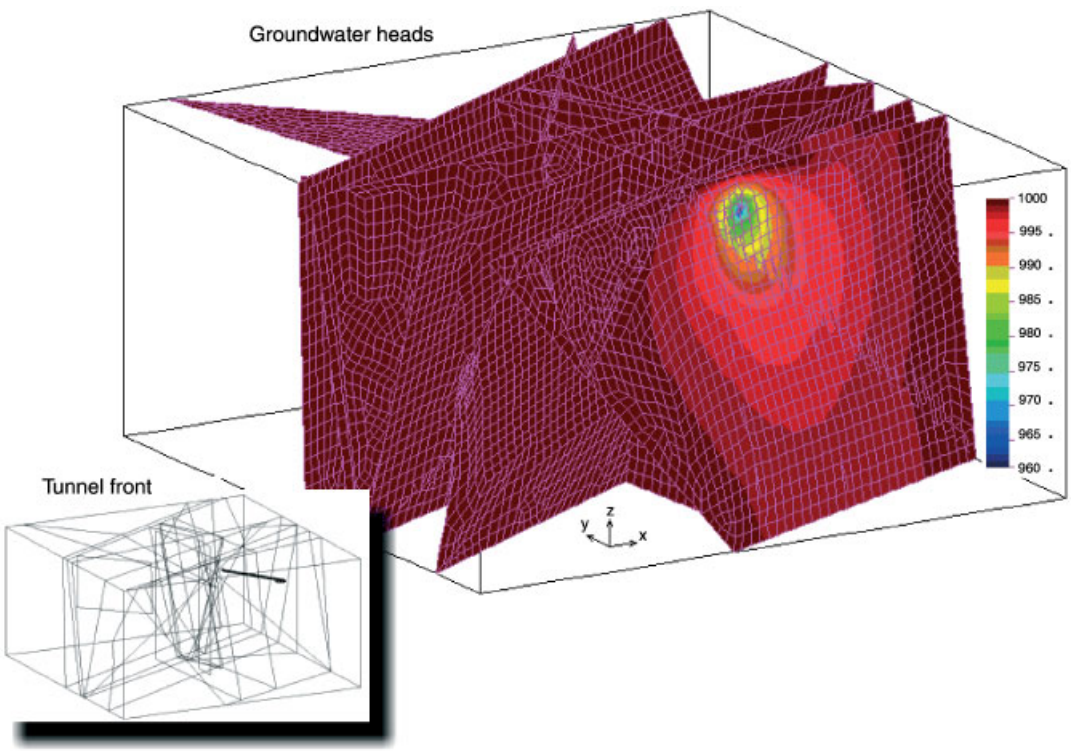

Plate 1. Groundwater system at the Äspö site. Predicted piezometric head after 133 days.

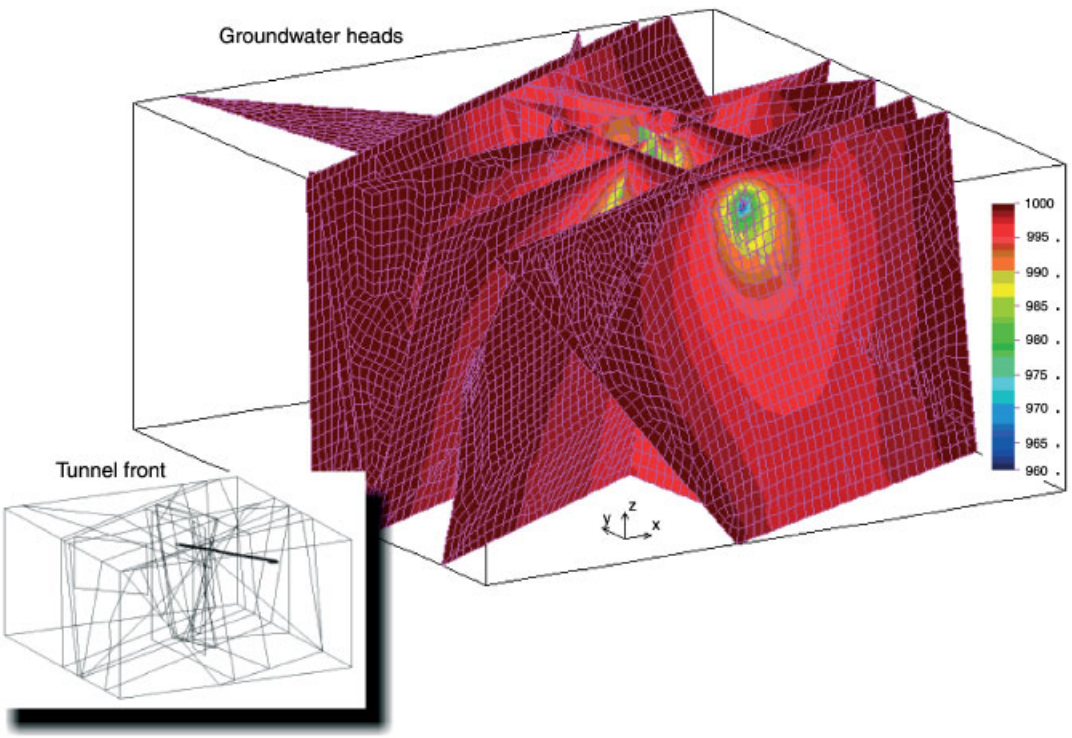

Plate 2. Groundwater system at the Äspö site. Predicted piezometric head after 423 days.

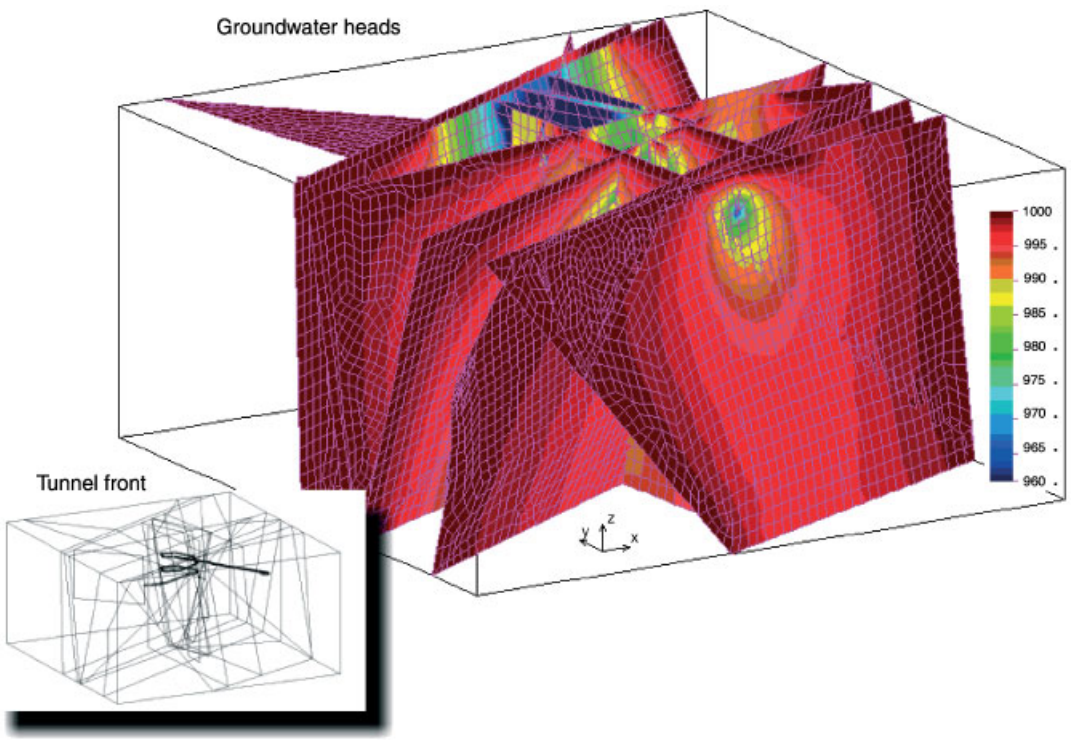

Plate 3. Groundwater system at the Äspö site. Predicted piezometric head after 2013 days.

Table III. Finite element grids used in the test case.

Identifier	# nodes	# elem.	Type of elements
M2D_2K	2112	2015	2D linear
M2D_6K	6105	5940	2D linear
M2D_20K	18 149	5940	2D quadratic
M1D_2K	2201	2314	2D & 1D linear
M1D_6K	6501	2314	2D & 1D quadratic
M1D_20K	19 705	6962	2D & 1D quadratic

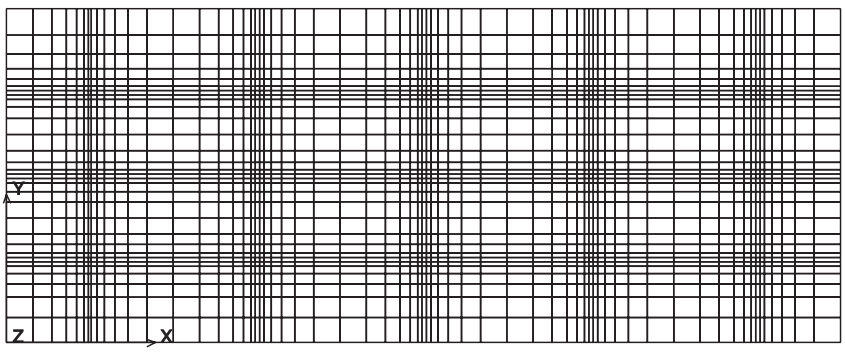

Figure 6. Finite element mesh for the 2D Model with 2112 nodes (M2D_2K in Table III).

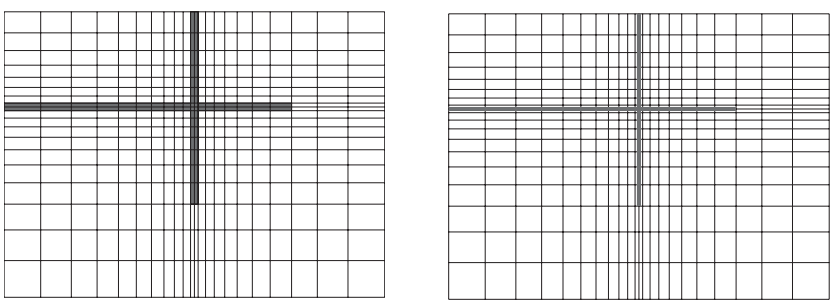

Figure 7. Detail of the finite element grids around fractures for the 2D Model with 18 149 nodes (left) and the 1D Model with 19 705 nodes (right).

The same time discretization has been used for all simulations: a Crank–Nicolson finite-difference scheme with a time step which increases gradually from $\Delta t = 0.1$ to 10 d.

All the simulations have been computed on a DIGITAL AlphaServer 4000 5/466 4MB with OpenVMS V7.1 operating system, at the Civil Engineering School of La Coruña University (Spain).

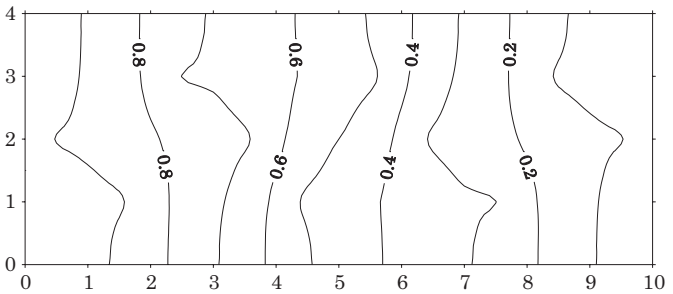

Figure 8. Contour plot of hydraulic heads computed using the 2D Model with 2 112 nodes (run M2D_2K).

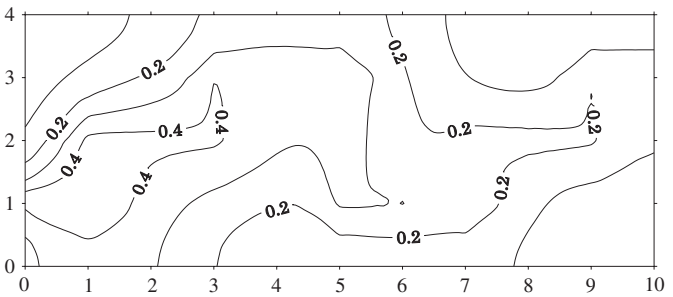

Figure 9. Contour plot of concentrations after 10 000 days using the 2D Model with 2112 nodes (run M2D_2K).

5.3. *Results*

The numerical solution of steady-state groundwater flow is discussed first. The contour plot of hydraulic head h obtained using the 2D Model with 2112 nodes (run M2D_2K) is shown in Figure 8. It is noticeable that the head contours are closer together in the regions of lower hydraulic conductivity (far away from the fractures). Solution using the 2D Model with 6105 nodes (run M2D_6K) differs from that of run M2D_2K only slightly, the maximum differences in pointwise values being about 1%. The contour plot for this simulation would look so similar to Figure 8 that it was not included. When the 1D Model is employed, the numerical solutions obtained with 2201-node and 6501-node grids (runs M1D_2K and M1D_6K, respectively) are virtually identical. Nodal values of these two simulations differ only after the fourth significant digit. The maximum discrepancies between the solutions of runs M2D_6K and M1D_6K are about 0.01%. Such a small difference suggests interpreting these results as 'engineering exact' solutions.

Contour plots of solute concentration after 10 000 days are shown in Figures 9–12. Concentrations computed using the 2D Model and a mesh of 2112 nodes (run M2D_2K, see Figure 9) differ significantly from those computed using the same model but with a finer mesh of 6105 nodes (run M2D_6K, see Figure 10). Such large differences in computed concentrations indicate clearly that the spatial discretization of run M2D_2K is not fine enough to obtain

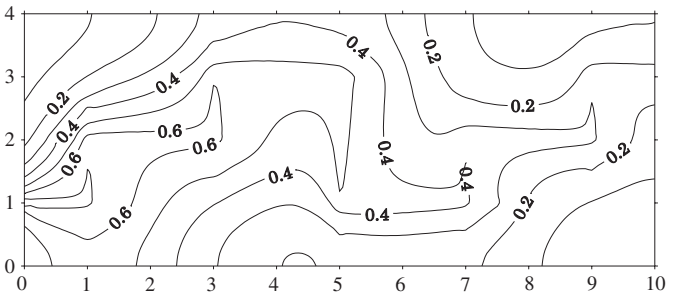

Figure 10. Contour plot of concentrations after 10 000 days using the 2D model with 6105 nodes (run M2D_6K).

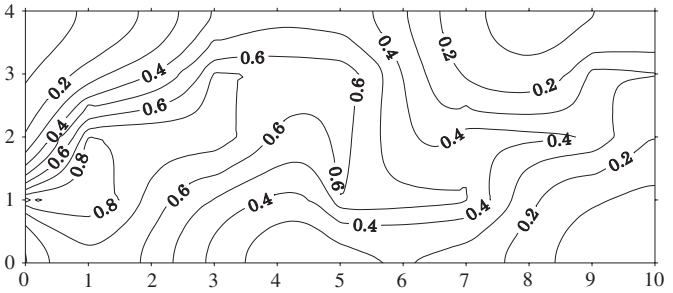

Figure 11. Contour plot of concentrations after 10 000 days using the 2D model with 18 149 nodes (run M2D_20K).

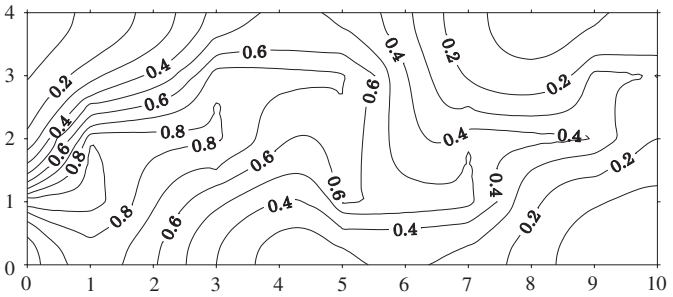

Figure 12. Contour plot of concentrations after 10 000 days using the 1D model with 2 201 nodes (run M1D_2K).

an accurate numerical solution. Numerical errors still persist with a grid of 6105 nodes, as one can see by comparing the numerical solutions obtained with 6105 nodes (Figure 10) and 18 149 nodes (Figure 11). Furthermore, the trend is not erratic: the finer the mesh, the larger the solute concentrations are throughout the domain (compare Figures 9–11). These results suggest that when the 2D Model is used to solve the solute transport equation, an extremely fine mesh is required to obtain accurate numerical solutions for heterogeneous systems.

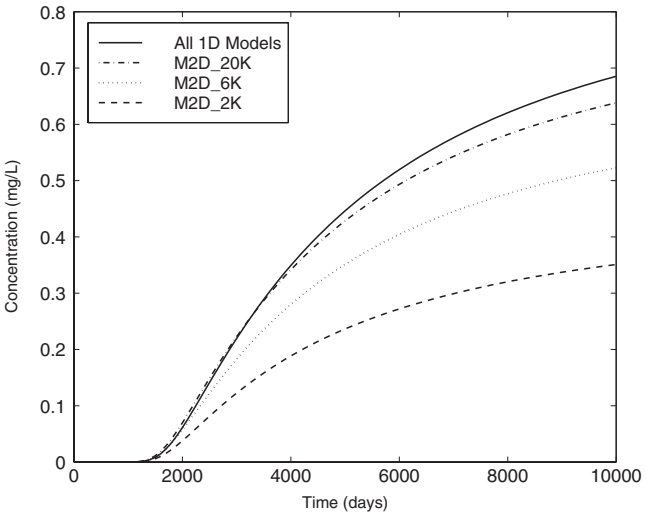

Figure 13. Breakthrough curves at the observation point. Comparison of all different simulations.

Results calculated using the 1D Model display a different behaviour. The actual numerical values of concentrations computed with a mesh of 2201 nodes (run M1D_2K in Figure 12) and a mesh of 6501 nodes (run M1D_6K) are different only after the third significant digit. These differences are so small that the plot of the concentrations of run M1D_6K has been omitted. As expected, the results of the simulation with 19 705 nodes (run M1D_20K) are virtually identical to those of run M1D_6K (discrepancies on the fourth significant digit).

Figure 13 shows the computed breakthrough curves (concentration versus time) at an observation point for all six aforementioned simulations. The observation point is located inside a fracture at the centre of the domain (see Figure 5). The curves corresponding to the 1D Model (runs M1D_2K, M1D_6K and M1D_20K) lie on top of each other, with maximum differences of 0.2%. Moreover, it should be noted that the numerical solutions obtained with the 2D Model approach the 1D Model solution as the mesh is refined.

Additional insight into the numerical performance of 1D and 2D Models can be gained from the analysis of concentration errors. Concentrations obtained using the 1D Model with 19 705 nodes (run M1D_20K) are regarded as the 'exact' solution. Dimensionless errors are computed for each run by taking the difference between concentrations obtained for that specific simulation and the exact solution, and dividing by the inlet concentration C_0, that is

$$\varepsilon_{\text{run}}(\mathbf{x},t)=\frac{C_{\text{run}}(\mathbf{x},t)-C_{\text{exact}}(\mathbf{x},t)}{C_0}$$

Contour plots of the dimensionless concentration errors after 10 000 days are shown in Figures 14–17. Errors corresponding to the 2D Model and a mesh of 2112 nodes (run M2D_2K, see Figure 14) are large over the entire domain and the maximum error is about 50%. Note that higher values occur along fractures and in the neighbourhood of the injection point, with error contours showing a pattern similar to that of the concentration itself (compare Figures 9 and 14). The contour plot of the errors for the 2D Model with a 6105 node mesh (run M2D_6K) is shown in Figure 15. The behaviour is very similar to that of run M2D_2K, with global

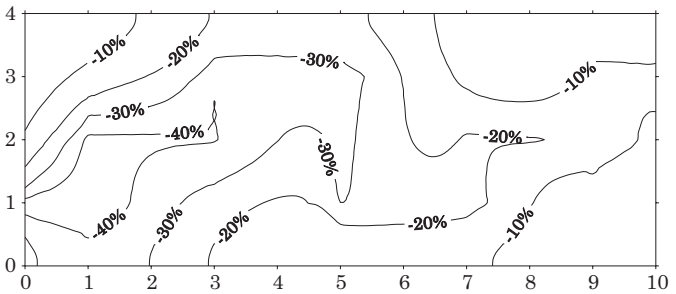

Figure 14. Contour plot of normalized concentration errors after 10 000 days for the 2D Model with 2112 nodes (run M2D_2K).

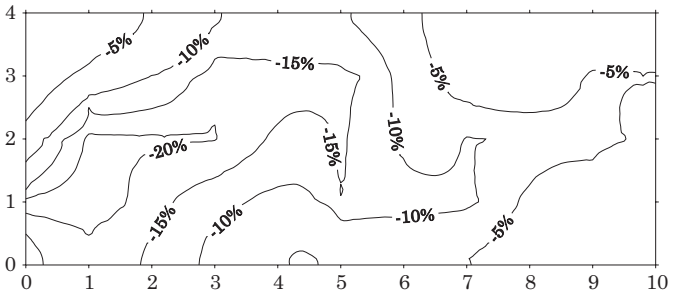

Figure 15. Contour plot of normalized concentration errors after 10 000 days for the 2D Model with 6105 nodes (run M2D_6K).

errors following the pattern of the concentration contours (compare Figures 10 and 15) and a maximum error close to 25%. Figure 16 shows the errors for the 2D Model with a mesh of 18 149 nodes (run M2D_20K). Even though the maximum error is reduced to 8%, the same comments above apply to this simulation. Figure 17 shows the normalized concentration errors obtained using the 1D Model with a 2201 node grid (run M1D_2K). Although a relatively coarse mesh is employed, the maximum error is about 2% and errors are noticeable only along the fractures. These results demonstrate the superior performance of the 1D Model, especially if one compares this solution to the 2D Model solution for a similar computational cost. The maximum error is 20 times lower, and the errors are restricted to the vicinity of fractures. Maximum concentration errors for the 1D Model with 6501 nodes (run M1D_6K) are of the order of 0.2%, and hence the figure with the error contours is not included.

Table IV shows memory requirements, CPU time, maximum error and mean error for all simulations. The mean error has been calculated as

$$\bar{\varepsilon} = \frac{1}{A} \int_{\Omega} \varepsilon(\mathbf{x})\, \mathrm{d}\mathbf{x}$$

It is remarkable that, for a similar computational cost, the errors associated with the 1D Model are several orders of magnitude lower than those of the 2D Model. For grids with roughly

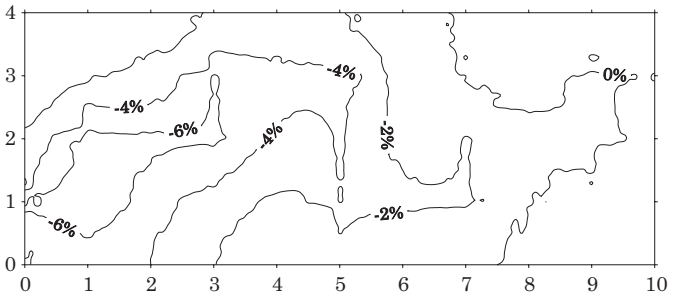

Figure 16. Contour plot of normalized concentration errors after 10 000 days for the 2D Model with 18 149 nodes (run M2D_20K).

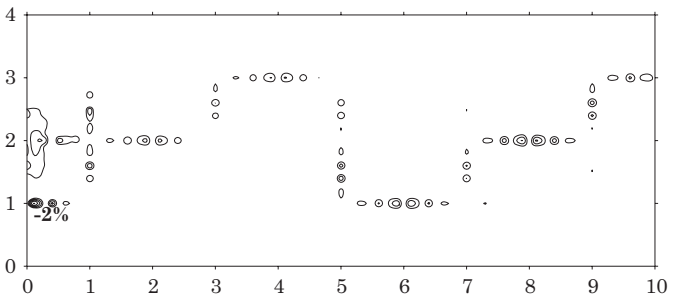

Figure 17. Contour plot of normalized concentration errors after 10 000 days for the 1D Model with 2 201 nodes (run M1D_2K).

Table IV. Memory, CPU time, maximum error and mean error of all simulations used in the test case.

Mesh identifier	Memory (MB)	CPU time (s)	Maximum error (%)	Mean error (%)
M2D_2K	4.2	46.9	−49.7	−20.4
M2D_6K	19.0	374.8	−24.2	−9.5
M2D_20K	159.6	3438.6	−8.0	−2.3
M1D_2K	4.7	50.5	−2.48	−0.16
M1D_6K	33.0	450.3	−0.21	−0.01
M1D_20K	196.4	4320.2	n/a	n/a

2000 nodes (runs M2D_2K and M1D_2K), the maximum error is reduced by a factor of 20 and the mean error by a factor of 100 when fractures are discretized using 1D elements. These factors are 100 and 1000, respectively, for grids with roughly 6000 nodes (runs M2D_6K and M1D_6K). Moreover, the 1D Model with a coarse grid (run M1D_2K) yields more accurate

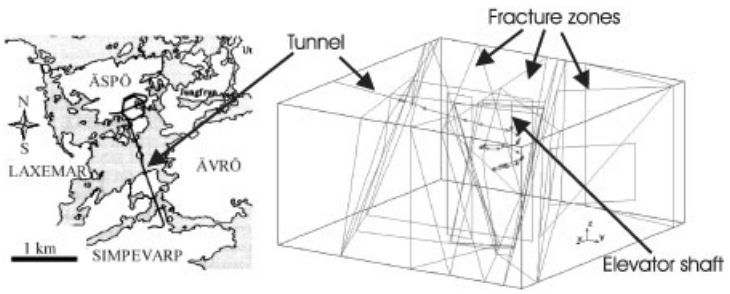

Figure 18. Left: location of the Äspö site with a plan view of the Äspö HRL. Right: geometry of the conceptual model, including fracture zones, the tunnel and the elevator shaft.

results than the 2D Model with an extremely fine grid (run M2D_20K), while cutting down the CPU time by a factor of 70.

From the results presented and discussed above, it can be concluded that the 1D Model proposed in this paper (in which fractures are discretized using 1D elements) provides much more accurate results with less computational cost than traditional finite elements (in which fractures are discretized with 2D elements) for the numerical solution of the solute transport equation in fractured media. The numerical analysis of the method and the explanation of its outstanding efficiency are the subject of future investigation.

6. REAL CASE: TUNNEL CONSTRUCTION IN A 3D FRACTURED ROCK

6.1. Introduction

The proposed formulation, which has been implemented in a computer code and tested with synthetic examples, has been applied also to real case studies. Here, its application to a problem dealing with groundwater flow induced by the construction of a tunnel in a granitic site at the Äspö Island (Sweden) is reported. The tunnel is part of the Äspö Hard Rock Laboratory (HRL), constructed and operated by the Swedish Nuclear Waste Company (SKB) within the framework of research programmes on radioactive waste disposal. The tunnel is 3600 m long and 450 m deep, and it consists of a straight ramp and a spiral in the final section (see Figure 18). The buildings and facilities on the surface are connected to the tunnel through an elevator. A detailed geological and hydrogeological characterization, performed by SKB, allowed the identification of the major fracture zones [15–17]. These studies point out at least 20 major fracture zones with a wide range of orientations, depicted in Figure 18. The conceptual hydrogeological model includes two main hydrogeological domains which have very different hydraulic properties: the rock domain and the conductive hydraulic domains [15, 17]. The density variations (due to salinity) can be disregarded because their effect on the groundwater system is negligible compared to that of hydraulic gradients induced by the construction of the tunnel [18]. This modelling exercise was useful to assess the impact of the tunnel construction on the groundwater system at the Äspö site and test the prediction capabilities of current numerical models.

6.2. Numerical model

A numerical model of groundwater flow and solute transport was carried out using the finite element programme TRANMEF-3 to simulate the impact of the tunnel construction on the hydrogeology of the Äspö Island [19, 20]. Owing to limitations of space, only the results of the flow model are presented here (see Reference [21] for details). The numerical model consists of 20 conductive hydraulic domains (which are discretized with 2D elements) and a tunnel (discretized with 1D elements), in a 3D domain of size $2 \times 2 \times 1\,\mathrm{km}^3$. Only 11 fractures actually intersect the tunnel, although there are 29 tunnel–fracture intersections, since some of the fracture zones cross the spiral section of the tunnel at several depths.

An unstructured finite element mesh was generated for the fractures using 2D bilinear quadrilateral elements. The mesh was refined in the neighbourhood of the intersections of the fractures and the tunnel using linear triangular elements. The tunnel and the elevator shaft were discretized with 1D linear finite elements. The final mesh consists of 12 847 nodes and 14 273 elements.

The time domain covers a period of 2013 days, from 1991/06/27 through 1997/01/01. A constant time step of $\Delta t = 1$ day was used. When the tunnel intersected a fracture, a smaller time step of $\Delta t = 0.1$ days was used for a period of several days following the intersection due to the fast transients occurring when the tunnel passes through a highly conductive zone.

Special attention was given to boundary conditions. On the bottom boundary, a no-flow (Neumann) boundary condition was imposed. The nodes on the side boundaries were set to a fixed piezometric head (Dirichlet). A Dirichlet boundary condition was used for nodes lying on the Baltic Sea, while a Neumann-type condition of specified recharge caused by rainfall was used for nodes along the top boundary lying on ground surface. A relevant feature of the model is its ability to accurately represent the inner moving boundary represented by the tunnel construction [22]. A time-dependent mixed (Cauchy) boundary condition was used for the nodes along the tunnel. Initially, the leakage coefficient α (see Table I) of these nodes is equal to zero. When the tunnel front reaches a node, its associated leakage coefficient takes a large positive value, therefore imposing the external piezometric head (which is equal to the elevation of that point since water pressure is equal to the atmospheric pressure). We can think of the leakage coefficient α varying in time as a Heaviside function, with its step located at a different time for each node on the tunnel. This allows one to perform a fully dynamic simulation of the impact of the tunnel on the groundwater system. The position of the advancing tunnel front was approximated using 29 stages, corresponding to each of the intersections of the tunnel with the fractures (Figure 19).

6.3. Results

Even though the geometric characteristics of the flow model were well defined, some calibration of the flow parameters (mainly hydraulic conductivity K and specific storage coefficient S_s) was needed. Calibration was especially difficult given the complex geometry of the problem and the large amount of available field data. A reasonably good agreement of model predictions and measured data was finally obtained in terms of:

1. Inflows into different sections of the tunnel (Figure 20).
2. Drawdowns at observation points (boreholes) located throughout the domain (Figure 21).

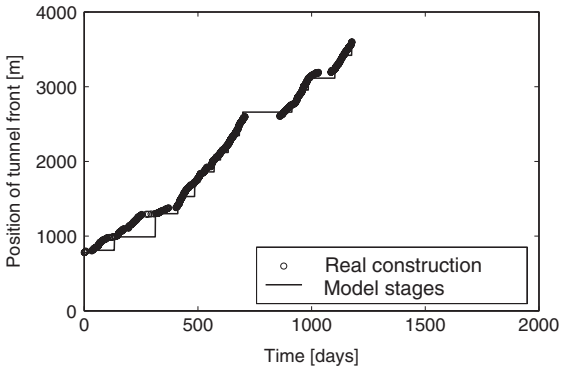

Figure 19. Tunnel construction. Actual location of the advancing front (circles) and the modelling stages (solid line).

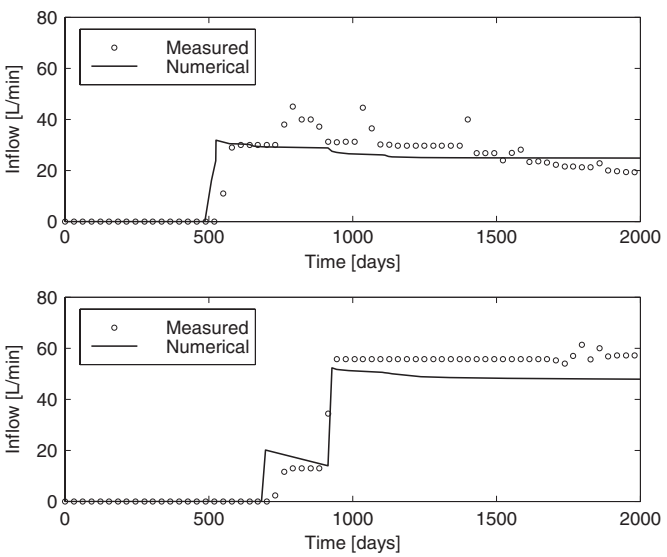

Figure 20. Inflow into the tunnel at two different control sections. Measured values (circles) and model predictions (solid line).

It is worth noting that calibrated values of hydraulic conductivity and specific storativity lie on the range of uncertainty of measured values.

Plates 1–3 show a three-dimensional representation of the evolution of piezometric head over the domain after 133, 423 and 2013 days, together with the position of the tunnel front. These figures exhibit the geometrical complexity of the problem. The results are meaningful and plausible, and they predict a generalized drawdown over the entire domain due to the construction of the tunnel. A thorough discussion of the results can be found in Reference [21].

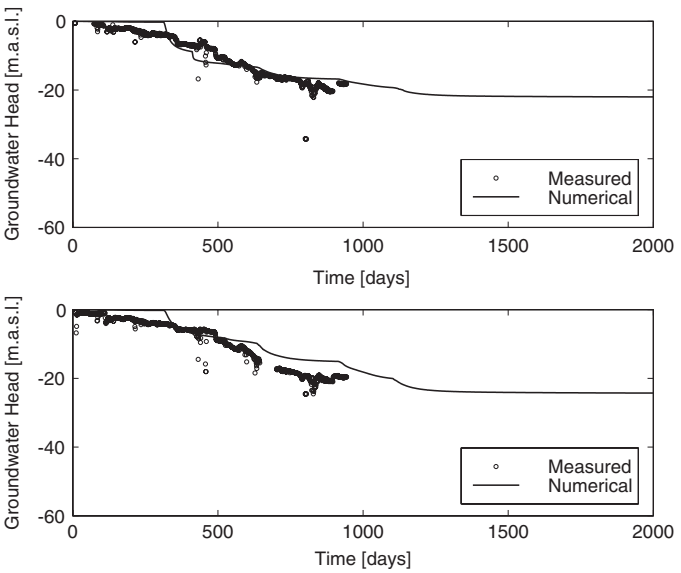

Figure 21. Piezometric heads at two different control points (boreholes). Measured values (circles) and model predictions (solid line).

7. CONCLUSIONS

A general and compact formulation for the implementation of fractures and boundary conditions in finite element models has been presented. It was first proposed in References [2, 3] and later revisited and generalized in Reference [5]. From a mathematical viewpoint, fractures are considered as m-dimensional manifolds in a n-dimensional Euclidean space ($m \leqslant n$). The key step of the formulation lies on an expression relating the hypersurface element $\mathrm{d}S_m$ to the infinitesimal local co-ordinates $\mathrm{d}\xi_1, \ldots, \mathrm{d}\xi_m$ (see Equation (14)). A novel proof for this relation has been provided. The formulation is valid for integration over elements of any dimension (e.g. 1D, 2D and 3D elements in a 3D domain) and overcomes the cumbersome calculations of traditional approaches. This provides a unified and elegant way to treat fractures embedded in a continuum in finite element codes.

The mathematical formulation has been implemented in a versatile finite element code for modelling groundwater flow, solute transport and heat transport in porous and fractured media [1, 6, 14].

The results of a 2D synthetic test case dealing with flow and transport through a block of fractured rock show the outstanding efficiency of the proposed formulation compared to the traditional finite element formulation, in which fractures are discretized with two-dimensional elements. The results of these test case, which are summarized in Table IV, indicate that for a given accuracy our formulation is much more efficient in terms of CPU time and memory requirements than the traditional method of treating fractures with 2D elements. On the other hand, for the same CPU time, the proposed formulation is remarkably more accurate than the standard finite element approach.

The capability of the proposed formulation to cope with the complexities of real problems has been illustrated with a case study of groundwater flow induced by the construction of the access tunnel to an underground research laboratory in Äspö (Sweden). The numerical model is able to reproduce the observed records of water levels in boreholes and flow rates into the tunnel.

Although the proposed formulation has been implemented and tested within the framework of groundwater flow and solute transport in fractured porous media, it should be of interest for other boundary value problems.

ACKNOWLEDGEMENTS

The work presented here has been funded by the Spanish Nuclear Waste Company (ENRESA), within an agreement between the University of La Coruña (Spain) and the Civil Engineering Foundation of Galicia: FEBEX Project (code 703231) and Code Validation Project (code 703334). The FEBEX Project has been partially funded by the European Commission through the Nuclear Fission Program (Project F14W-CT95-0006). Partial funding has also been provided by the CICYT through the Spanish Program in Water Resources (Project HID98-282). Access to the Äspö HRL data has been possible thanks to the agreement between ENRESA (Spain) and SKB (Sweden). The authors are grateful to Barrié de la Maza Foundation and the Spanish Ministry of Science and Education for the research fellowships awarded to the first and third authors, respectively. The authors are thankful to the reviewers for their valuable comments.

REFERENCES

1. Juanes R, Samper J. Una formulación general y eficiente de fracturas y condiciones de contorno en el M.E.F.: I. Aspectos teóricos, *Revista Internacional de Métodos Numéricos para Cálculo y Diseño en Ingeniería* 2000; **16**(4):471–491.
2. Kiraly L. Remarques sur la simulation des failles et du réseau karstique par éléments finis dans les modèles d'écoulement. *Bulletin du Centre d'Hydrogéologie* 1979; **3**:155–167 (University of Neuchâtel, Switzerland).
3. Kiraly L. Large scale 3-D groundwater flow modelling in highly heterogeneous geologic medium. In Custodio E, Gurgui A, Ferreira JP. (eds), *Groundwater Flow and Quality Modeling* Reidel: Dordrecht, 1987; 761–775.
4. Kirmmeier F, Perrochet P, Andrews R, Kiraly L. Simulation des écoulements souterrains entre les Alpes et la Forêt Noire par modèle mathématique. *Technical Report NTB* 84-50, NAGRA, 1985.
5. Perrochet P. Finite hyperelements: a 4D geometrical framework using covariant bases and metric tensors. *Communications in Numerical Methods in Engineering* 1995; **11**(6):525–534.
6. Juanes R. Un modelo numérico tridimensional de flujo y transporte: Desarrollo y aplicación de un código de elementos finitos para la solución de las ecuaciones de flujo subterráneo, transporte de solutos reactivos y transporte de calor en medios porosos y fracturados tridimensionales. Masters Thesis, Escuela Técnica Superior de Ingenieros de Caminos, Canales y Puertos, Universidad de La Coruña, May 1997.
7. Brenner SC, Scott LR. *The Mathematical Theory of Finite Element Methods*. Texts in Applied Mathematics, vol. 15. Springer: New York, 1994.
8. Ciarlet PG, Lions JL (eds). Finite Element Methods (Part 1), *Handbook of Numerical Analysis*, vol. II. Elsevier: North-Holland, 1991.
9. Thomée V. Galerkin Finite Element Methods for Parabolic Problems. *Springer Series in Computational Mathematics*, vol. 25. Springer: Berlin, 1997.
10. Zienkiewicz OC, Taylor RL. The Finite Element Method: (I) *Basic Formulation and Linear Problems*, (II) *Nonlinear Problems*, McGraw-Hill: New York, 1989.
11. Courant R, John F. *Introduction to Calculus and Analysis*, vol. 2. Wiley: New York, 1974.
12. Browder A. *Mathematical Analysis*: *an Introduction*. Undergraduate Texts in Mathematics. Springer: New York, 1996.
13. Teichmann H. *Physical Applications of Vectors and Tensors*. Harrap: London, 1969. (Translation by C. W. Kilmister).
14. Juanes R, Samper J. Una formulación general y eficiente de fracturas y condiciones de contorno en el M.E.F.: II. Aplicación a casos sintéticos, *Revista Internacional de Métodos Numéricos para Cálculo y Diseño en Ingeniería*, 2001; **17**(1):67–82.

15. Rhén I, Gustaffson G, Stanfors R, Wikberg P. Äspö Island models based on site characterization. *Technical Report TR* 97-06. Swedish Nuclear Fuel and Waste Management Co. (SKB) 1997.
16. SKB. Äspö Hard Rock Laboratory. Annual Report 1995. *Technical Report TR* 96-06. Swedish Nuclear Fuel and Waste Management Co., 1996.
17. Smellie JAT, Laaksoharju M, Wikberg P. Äspö, SE Sweden: a natural groundwater flow model derived from hydrochemical observations. *Journal of Hydrology* 1995; **172**:147–169.
18. Hautojärvi A, Koskinen L, Löfman P. Hydraulic modelling of the large scale redox experiment at Aspö HRL. *Progress Report PR*-25-94-37. Swedish Nuclear Fuel and Waste Management Co. (SKB), 1994.
19. Molinero J, Samper J, Juanes R. Three-dimensional numerical models of groundwater flow and solute transport in fractured granites: impact of tunnel construction in the groundwater system at the Aspö Island (Sweden). In Sililo O *et al*. (eds), *Groundwater*: *Past achievements and Future Challenges*, Cape Town (South Africa), XXX Congress of the IAH: 26 November–1 December 2000; 407–411.
20. Molinero J, Samper J, Juanes R, Buján L, Zhang G. Numerical modelling of the impact of the tunnel construction on the groundwater system at Aspö. *Progress Report*. Äspö Hard Rock Laboratory, Task Force #5, 1999.
21. Molinero J. Testing and validation of numerical models of groundwater flow, solute transport and chemical reactions in fractured granites: a quantitative study of the hydrogeological and hydrochemical impact produced by the construction of the Aspö Underground Laboratory (Sweden). *Ph.D. Dissertation*. Escuela Técnica Superior de Ingenieros de Caminos, Canales y Puertos. Universidad de La Coruña: Spain, July 2000.
22. Molinero J, Samper J, Juanes R. Numerical modeling of the transient hydrogeological response produced by tunnel construction in fractured bedrocks. *Engineering Geology* 2002; **64**(4):369–386.

